Supporting Information

Introducing atomistic dynamics at van der Waals surfaces for enhancing thermoelectric performance in layered $Bi_{0.4}Sb_{1.6}Te_3$

Adil Mansoor[a‡], Bushra Jabar[b‡], Syed Shoaib Ahmad Shah[c], Muhammad Sufyan Javed[d], Tayyaba Najam[a], Muhammad Ishaq[a], Shuo Chen[a], Fu Li[a], Xiao-Lei Shi[e], Yue-Xing Chen[a], Guang-Xing Liang[a], Zhi-Gang Chen[e], Zhuang-Hao Zheng[a]*

[a] Shenzhen Key Laboratory of Advanced Thin Films and Applications, Key Laboratory of Optoelectronic Devices and Systems of Ministry of Education and Guangdong Province, State Key Laboratory of Radio Frequency Heterogeneous Integration, College of Physics and Optoelectronic Engineering, Shenzhen University, Shenzhen, Guangdong 518060, China

[b] Institute for Metallic Materials, Leibniz Institute for Solid State and Materials Research Dresden, 01069 Dresden, Germany

[c] Department of Chemistry, School of Natural Sciences, National University of Sciences and Technology, Islamabad, 44000 Pakistan

[d] School of Physical Science and Technology, Lanzhou University, Lanzhou, 730000, China

[e] School of Chemistry and Physics and Centre for Materials Science, Queensland University of Technology, Brisbane, Queensland 4001, Australia

[‡] These authors contributed equally to this work.

* Corresponding author: zhengzh@szu.edu.cn

Table of Contents

Supplementary Note 1: Details on structure of N-C doped $Bi_{0.4}Sb_{1.6}Te_3$ system

In this work, the layered $Bi_{0.4}Sb_{1.6}Te_3$ material is selected as the demonstrative to reconnoiter the preparation and growth mechanism under doping. Additionally, the potential application of porous Nitrogen-doped Carbon (N-C) as a nano-filler in optimizing the thermoelectric performance for $Bi_{0.4}Sb_{1.6}Te_3$ is investigated. The synthesis temperature of bulk $Bi_{0.4}Sb_{1.6}Te_3$ material was modified based on the porous N-C. The synthesis process for doped $Bi_{0.4}Sb_{1.6}Te_3$+x(N-C) system (x= 0, 0.05, 0.10, 0.15, 0.20, and 0.25 wt.%) is mentioned in the experimental section (as given in supplementary note 7).

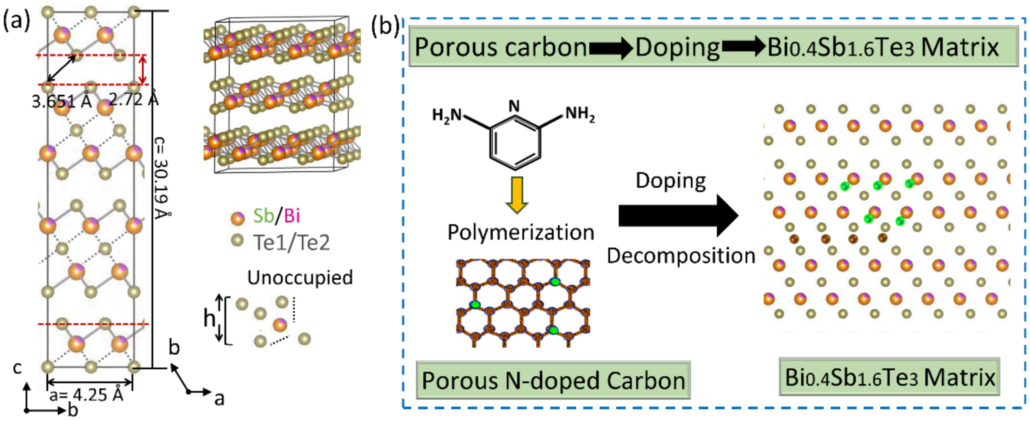

Fig. S1 (a) Schematic presentation for $Bi_{0.4}Sb_{1.6}Te_3$; (b) a directional guide view for selective strategy for doped $Bi_{0.4}Sb_{1.6}Te_3$+x(N-C) system (x= 0, 0.05, 0.10, 0.15, 0.20 and 0.25 wt.%).

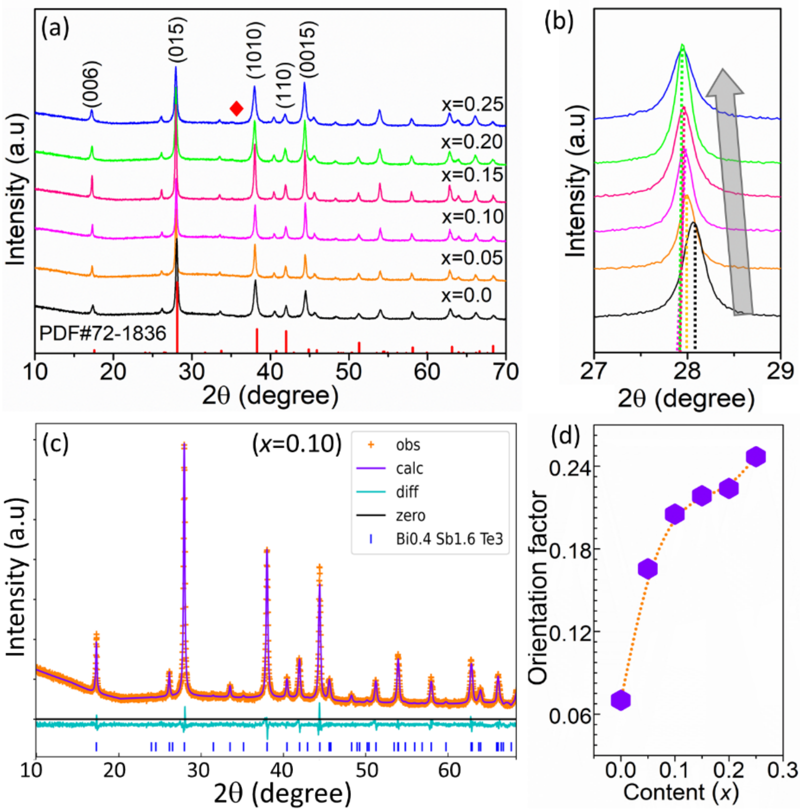

Fig. S2 (a) XRD patterns for all doped $Bi_{0.4}Sb_{1.6}Te_3$+x(N-C) system (x= 0, 0.05, 0.10, 0.15, 0.20 and 0.25 wt.%); (b) enlarged view at selective angles for all the samples; (c) GSAS driven pattern for doped $Bi_{0.4}Sb_{1.6}Te_3$ sample (at x= 0.15); (d) orientation factor for present N-C doped $Bi_{0.4}Sb_{1.6}Te_3$ (x= 0, 0.05, 0.10, 0.15, 0.20 and 0.25) structure.

Fig. S2 depicts XRD patterns for synthesized pristine and N-C doped $Bi_{0.4}Sb_{1.6}Te_3$ system. Fig. S2a shows the XRD peaks of all specimens are well consistent with the hexagonal pattern of $Bi_{0.4}Sb_{1.6}Te_3$ phase (JCPDS#: 072-1836) under different doping. Further, refinement analysis also confirms that a high-quality $Bi_{0.4}Sb_{1.6}Te_3$ pure hexagonal phase was obtained under the optimized heating process and doping (Fig. S3). With the increase of doping, a change in lattice parameters (Figs. S2-S4), peak shifting toward lower angle (Figs. S2b & S3), and a fluctuation in the interatomic distance indicates the presence of lattice disparity in crystalline material (Figs. 3j-l & S4a-c) and demonstrate the variations in structural environment of host $Bi_{0.4}Sb_{1.6}Te_3$ material under C and N doping (Figs. 2-3 & S2-S4).

Additionally, the (00l) diffraction exhibits high intensities with doping, indicating the presence of the (00l)-oriented texture after doping. For instance, the orientation factor (F) upsurges as of 0.07 to 0.25 as doping rises from x=0.00 to x= 0.25 wt.% (Fig. S2d). Here, the variation in interatomic bonding/distance depicts the existence of lattice variations upon doping. Further, the experimental and simulation-based analysis explains the behavior of N-C doping on the structure of host p-type $Bi_{0.4}Sb_{1.6}Te_3$ material.

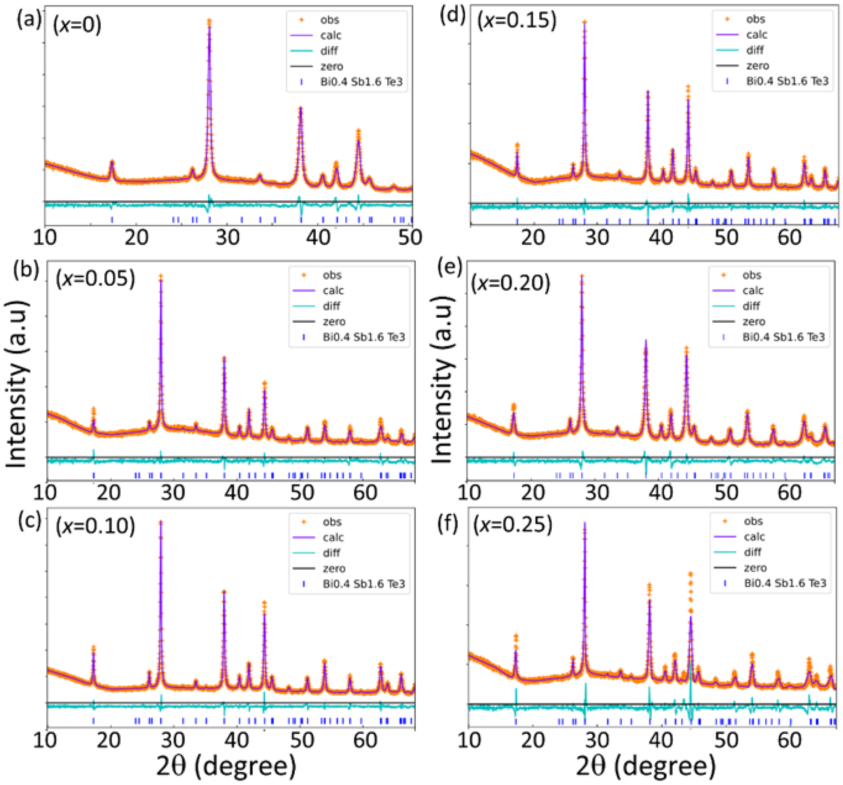

Fig. S3 Rietveld refinement analysis for doped $Bi_{0.4}Sb_{1.6}Te_3$+x(N-C) system: (a) x= 0; (b) 0.05; (c) 0.10; (d) 0.15; (e) 0.20; (f) 0.25 wt.%) samples. Here obs, calc, and diff are used to express the terms of observed, calculated, and residual among the simulated and measured data curves.

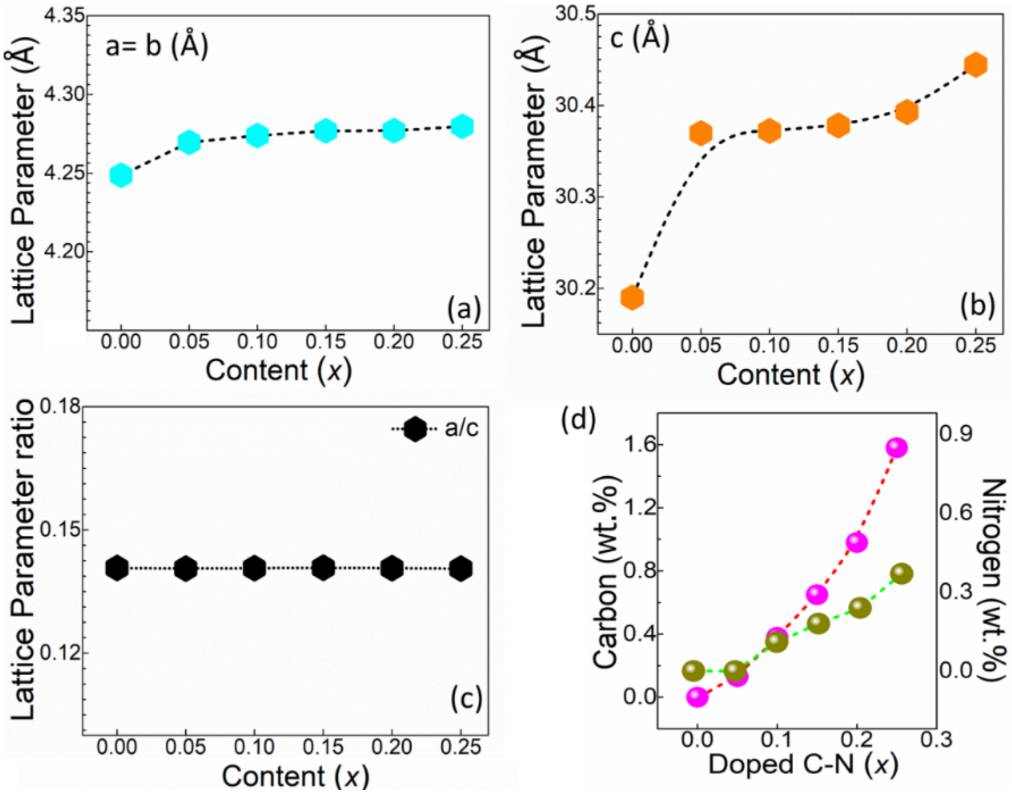

Fig. S4 (a) Lattice parameters for N-C doped $Bi_{0.4}Sb_{1.6}Te_3$ system (x= 0, 0.05, 0.10, 0.15, 0.20, 0.25wt.%) samples; (b) variation in lattice parameters for doped samples; (c) variation in unit cell volume for doped samples; (d) SEM-EDX derived content for N-C doped $Bi_{0.4}Sb_{1.6}Te_3$ shows variation in C and N content in N-C doped $Bi_{0.4}Sb_{1.6}Te_3$ samples.

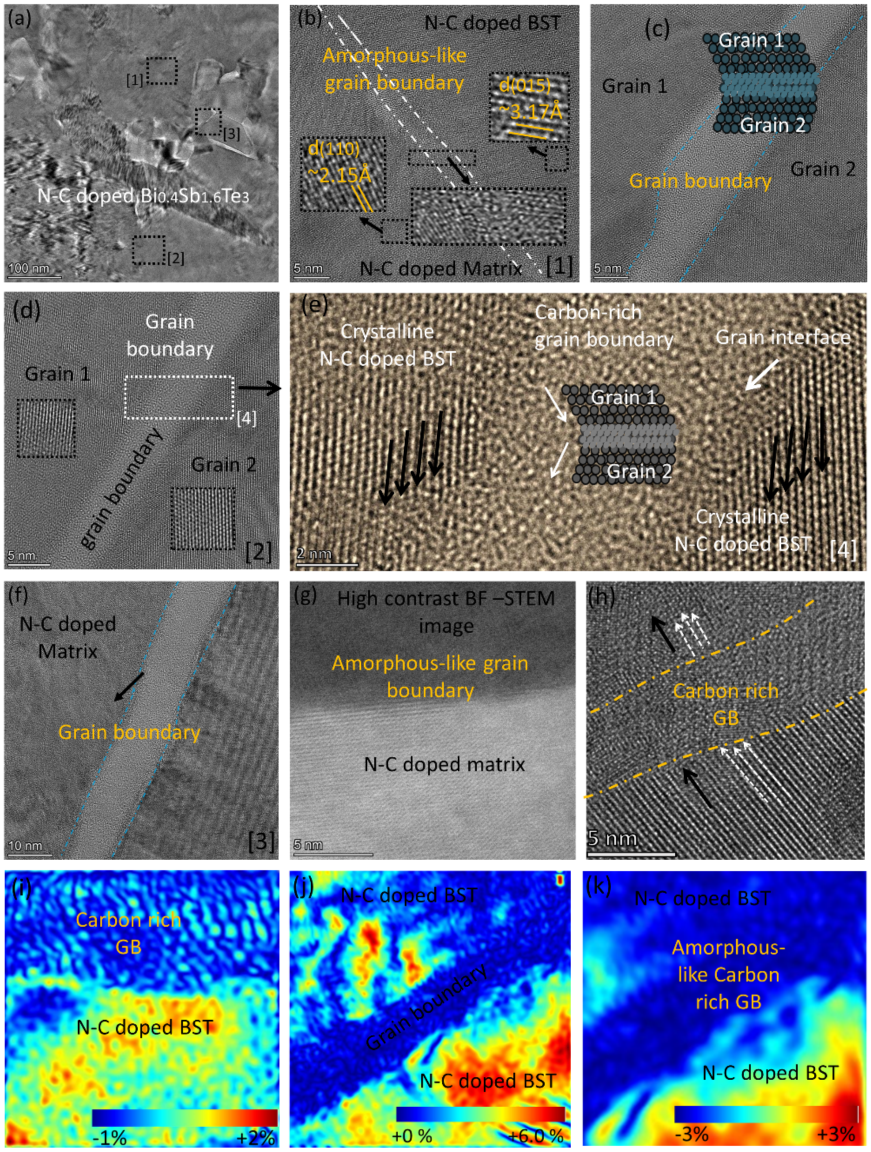

Fig. S5 (a) Low-resolution TEM micrograph showing embedded grain phase boundaries; (b) enlarged high-resolution STEM micrograph from the black rectangle area [1] in Fig. S5a; (c) HAADF-STEM amorphous grain boundary between two crystalline matrix grains; (d) high-resolution STEM micrograph of rectangle area [2] in Fig. S5a; (e) an enlarged micrograph view from the white rectangle area in Fig. S5d through Inverse Fast Fourier Tramsform (IFFT) approach depicts an amorphous grain boundary between two crystalline matrix grains; (f) ADF-STEM micrographs, which depicts amorphous grain boundary between two crystalline matrix grains; (g) high contrast ABF-STEM micrographs, which depicts amorphous grain boundary and a crystalline matrix grain at different contrast; (h) high resolution HAADF-STEM micrographs, which depicts amorphous grain boundary between two crystalline matrix grains; (i-k) the calculated strain profile map from the micrographs Figs. S5g, S5d, and S5h, respectively (therein, the included color scale shows the scale of strain in/around the matrix).

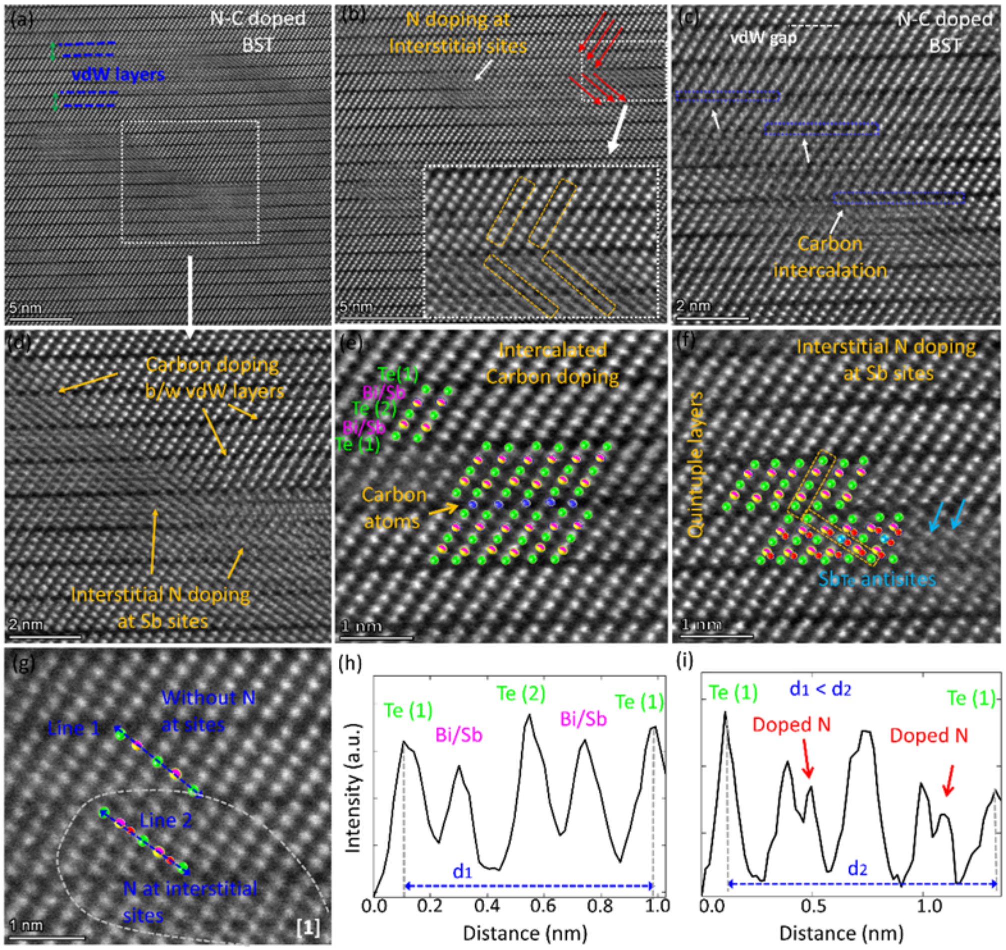

Fig. S6 (a-g) C-S corrected HAADF-STEM analysis for vdW inversion in N-C doped $Bi_{0.4}Sb_{1.6}Te_3$ system, where the stacking disorder can be clearly observed between normal QLs and Inverted QLs. The C intercalation and N interstitial doping-induced ordering of atomic blocks work as a reason behind the inversion of the atomic block; (h-i) the image intensity profile measurements along the vertical direction (indicated by blue line 1 & 2 in Fig. S5g) shows that variations in the width of the atomic block between the normal and inverse QLs.

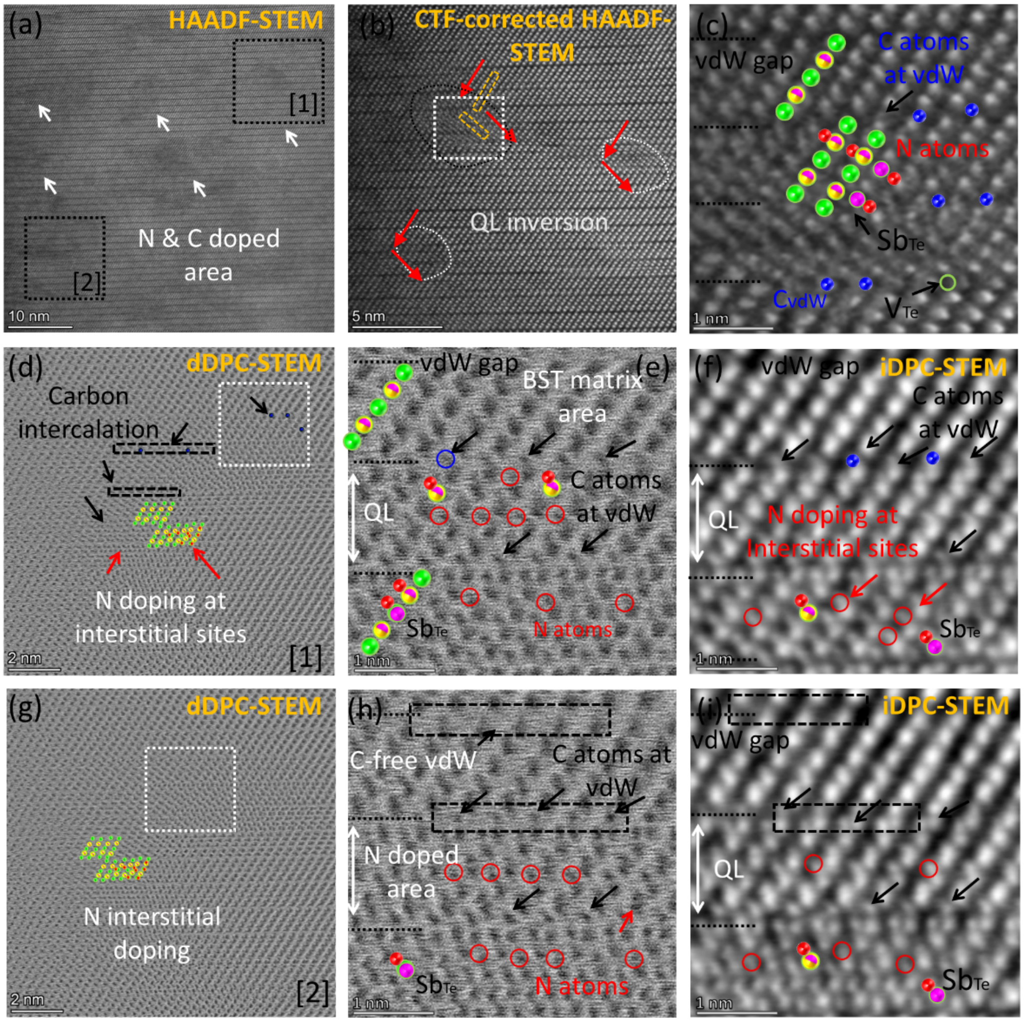

Fig. S7: (a) HAADF-STEM micrograph of N-C doped $Bi_{0.4}Sb_{1.6}Te_3$ (at x=0.15) system; (b) CTF-corrected HAADF-STEM micrograph, where the stacking disorder/inversion can be clearly observed between normal QLs and Inverted QLs; (c) enlarged ADF-STEM micrograph view of area marked by white rectangle in (b); (d) ABF dDPC-STEM micrographs for distribution/variations in interlayer and intralyers regions from the marked area [1] in (a); (e) CTF corrected dDPC-STEM image of area marked by white rectangle in (d) to magnify the N & C doped area; (f) iDPC-STEM based micrographs for doping-dependent intralyer variations within the quintuple layers (Te_{ε}-Sb-Te-Sb-Te_c); (g) ABF dDPC-STEM micrographs for distribution/variations in interlayer and intralyers regions from the marked region [2]; (h) CTF corrected dDPC-STEM image of area marked by white rectangle in (g); (i) iDPC-STEM micrographs for N & C atoms doped in $Bi_{0.4}Sb_{1.6}Te_3$ system.

Supplementary Note 2: Proposed defects in N-C doped $Bi_{0.4}Sb_{1.6}Te_3$ phase

All proposed defects such as atomic vacancy, interstitial, anti-site doping, and the position of possible C and N phase in N-C doped $Bi_{0.4}Sb_{1.6}Te_3$ system were derived through the DFT calculations. The analyzed possible behaviors of C and N atom in a doped $Bi_{0.4}Sb_{1.6}Te_3$ system includes Carbon and Nitrogen atoms replacement on the Sb atom (C_{Sb}, N_{Sb}), occupying vdW intercalation (C_{vdW}, N_{vdW}), replacing the Te atom (C_{Te}), occupying Sb cation vacancy (C_V), and interstitial doping (C_i, N_i) were inspected. Based on this analysis, the calculated and compared formation energy (E_{for}) of guest atoms in $Bi_{0.4}Sb_{1.6}Te_3$ depicts the possible doping trend of C and N doping in layered system. E_{for} is derived by; $\Delta E_{for}(A) = E_{tot}(A) - E_{tot}(bulk) + \Sigma_i n_i \mu_i$. $E_{tot}(A)$, $E_{tot}(bulk)$ and $E_{tot}(A)$ represents total energies from pristine and doped supercells, respectively. n_i represents the number of doped atoms, where $n_i > 0$ represents atomic substitution, and $n_i < 0$ represents removal of atom from the system the chemical potential of Se and Br. μ_i stands for chemical potential for the i atom. The computational results demonstrate that the E_{for} for carbon doping on all proposed position for $Bi_{0.4}Sb_{1.6}Te_3$ is very high, as shown in Fig. 2r & Fig. 3n (indicating that the carbon doping on atomic sites is not favorable). Furthermore, the distribution of carbon inside the bulk host system was explored for three possible situations; 1) random distribution of C inside system, 2) a long chain of carbon atoms at grain boundaries, and 3) a short chain of carbon atoms at grain boundaries in the host system. As seen, the randomly dispersed carbon atom (in crystal structure) has higher formation energy (Fig. 2r). The situation under long chain carbon atom accumulation on grain boundaries has shown very low formation energy. Thus, it can be predicted that the carbon atoms (above the solubility limit for doping) form carbon atomic clusters. Furthermore, the evaluation of the formation energy for possible sites in the present system suggests that C atoms prefer to intercalate at vdW gaps instead of occupying Sb/Te atomic or filling positions.

Supplementary Note 3: Determination of S dependency on the carrier concentration and other physical parameters.

Following the Mott formula, the variation of $|S|$ can be related mainly to the electron concentration. However, S is known to be determined by the *p* and other physical parameters.

The simply written expression as $S = S(p, N(E), \lambda, T)$ shows that if N(E), λ and T are kept as constants, S should decline with aggregate carrier concentration p, as projected by the Pisarenko relation. However, if N(E) or λ is altered (amplified), the S tracks (increased compared to the pristine system) will diverge from the Pisarenko relation (as shown in Fig. 5d). Thus, the deviation in S value from the Pisarenko relation is a condition of expression that the modification in electronic density of states N(E) fluctuations expressively in doped material.[1, 2] With doping (for $0.05 \leq x \leq 0.25$), the unconventionality of the S data over the calculated Pisarenko line (S, p) shows that the N(E) variations due to the stimulation of VB (Fig. 4). In addition, a change in the values of the m_d* mass with increasing x results from the disparity in lattice inversion, electronic structure, and crystal imperfections (Fig. S11e). In particular, the increase in m_d* implies variations in DOS. Explicitly, an increase in m_d* infers a non-parabolic perturbation for carrier scattering relations, i.e. an impurity or resonance level near E_f. The enhanced m_d* also specifies the robust alteration in DOS near E_f, as m_d* and DOS holds directly dependence (via a relation; $N(E) = \{4\pi(2(m^*_d)^{3/2} E^{1/2}\}/h^3$). Here, the origin of the DOS distortion is related to the N-C doping as described by the first principal calculations. The simulation results specify that N-C doping induces projecting impurity peaks adjacent to the E_f. The high-pitched impurity level/peak directs a higher m_d* and S in N- C doped system due to distortion-induced structural disparity.

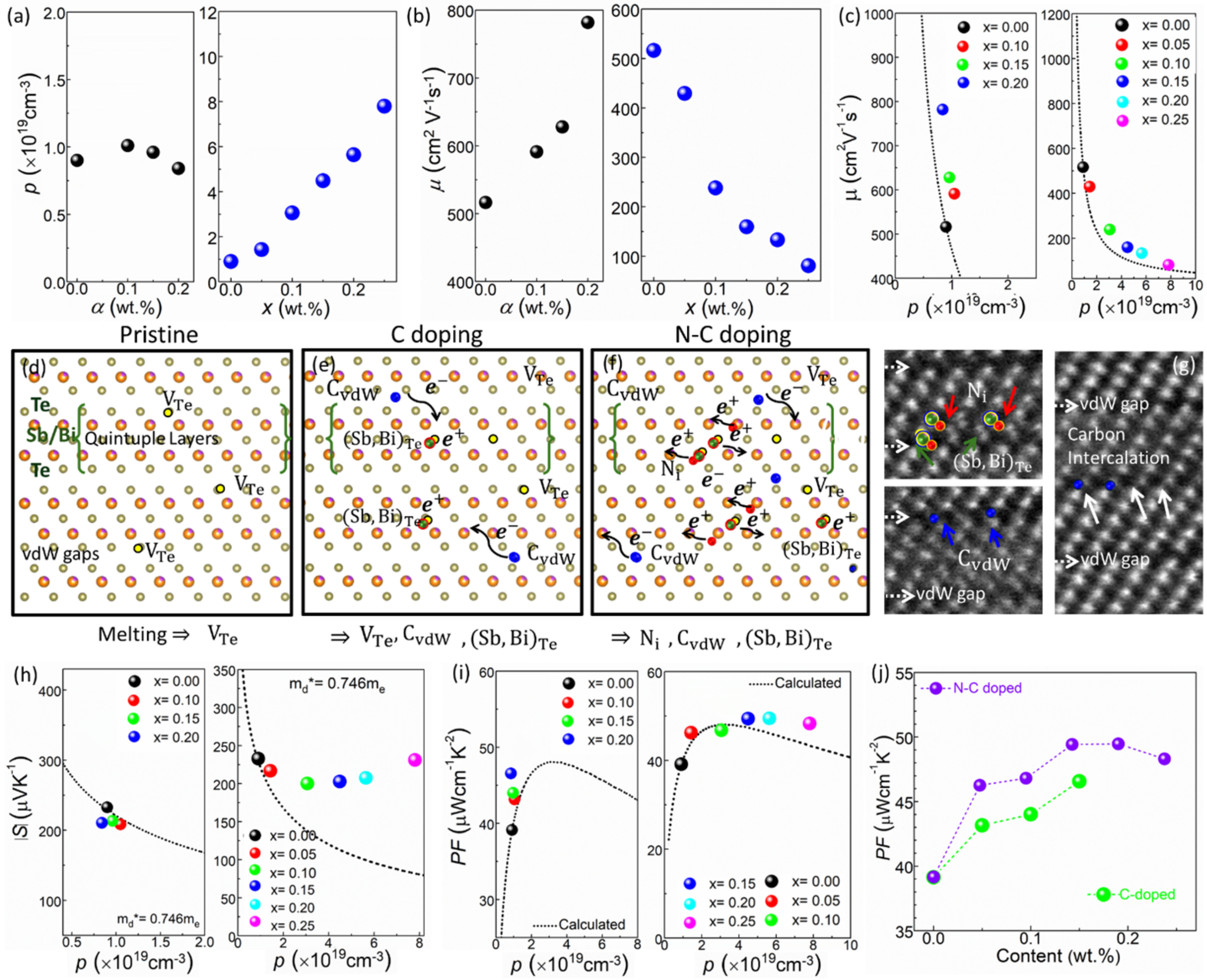

Fig. S8: A comparative trend in doped $Bi_{0.4}Sb_{1.6}Te_3+\alpha C$ (α= 0.00, 0.10, 0.15, 0.20) and doped $Bi_{0.4}Sb_{1.6}Te_3$+x(N-C) system (x= 0, 0.05, 0.10, 0.15, 0.20 and 0.25): (a) carrier concentration (*p*); (b) carrier mobility (μ); (c) *p*(μ) trend; (d)-(f) a schematic presentation of doping induced defect formation in the doped systems; (g) HAADF-STEM image indicating induced defects in the N-C doped system; (h) the dependency of S over *p* (at 300 K) derived by the SPB model; (i) the PF over *p* trend (at 300 K); (j) a comparison of PF in doped $Bi_{0.4}Sb_{1.6}Te_3+\alpha C$ (α= 0.00, 0.10, 0.15, 0.20) and doped $Bi_{0.4}Sb_{1.6}Te_3$+x(N-C) system (x= 0, 0.05, 0.10, 0.15, 0.20 and 0.25).

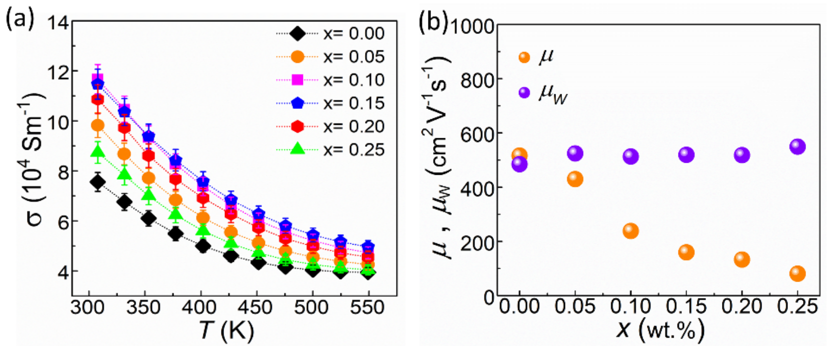

Fig. S9 (a) Temperature dependence trend of σ; (b) a comparison for electronic mobility (μ) and weighted mobility ($μ_W$) dependency on doping content (at *T*= 300 K).

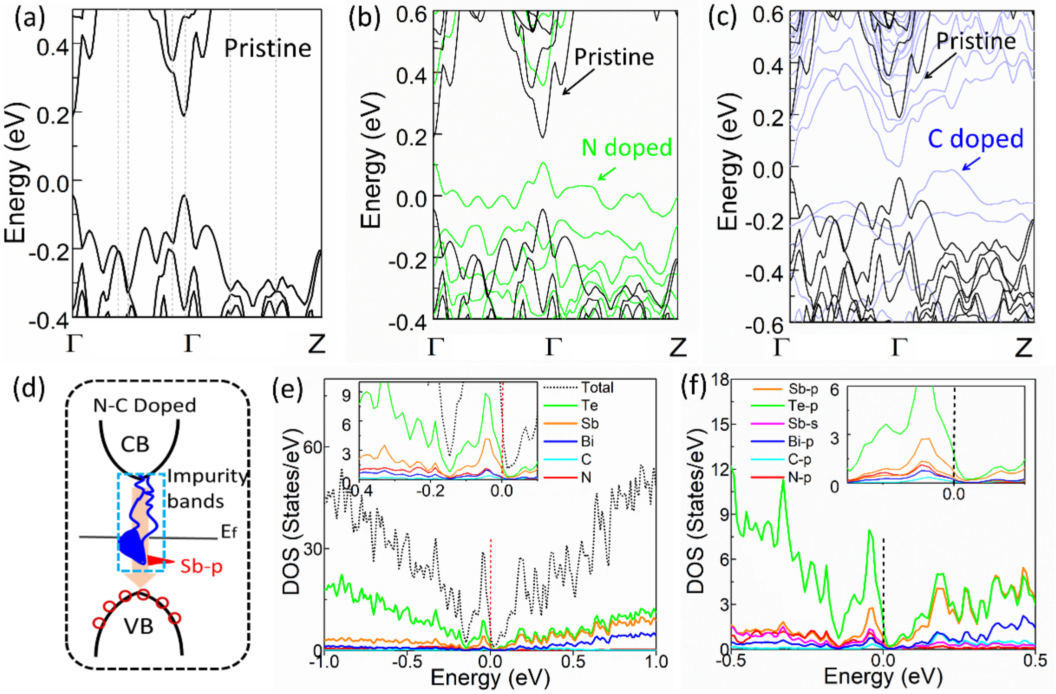

Fig. S10 (a) Electronic band structure of pristine $Bi_{0.4}Sb_{1.6}Te_3$ system; (b) a comparative band profile for pristine and N doped system; (c) a comparative band profile for pristine and C doped $Bi_{0.4}Sb_{1.6}Te_3$ system; (d) a schematic presentation of localized states; (e)-(f) PDOS profile N-C doped $Bi_{0.4}Sb_{1.6}Te_3$ system.

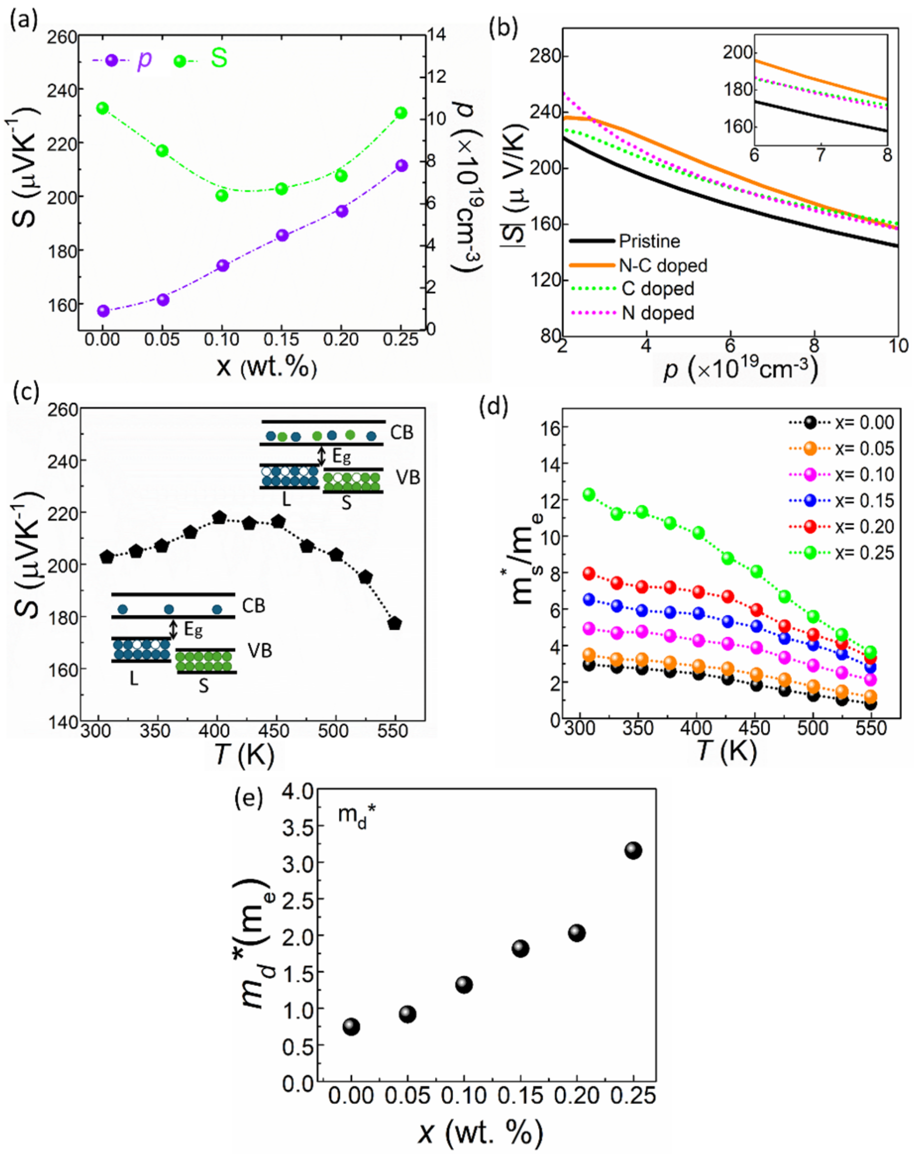

Fig. S11 (a) The computational analyzed S values over p curves for doped system (at 300 K); (b) DFT driven relation of S and p under doping dependent trend (at 300 K); (c) a presentation for variations in S under *T*; (d) S driven m_S* at different temperatures for N-C doped $Bi_{0.4}Sb_{1.6}Te_3$ specimens; (e) values of the m_d* mass derived from SPB model under doping dependent trend (at 300 K).

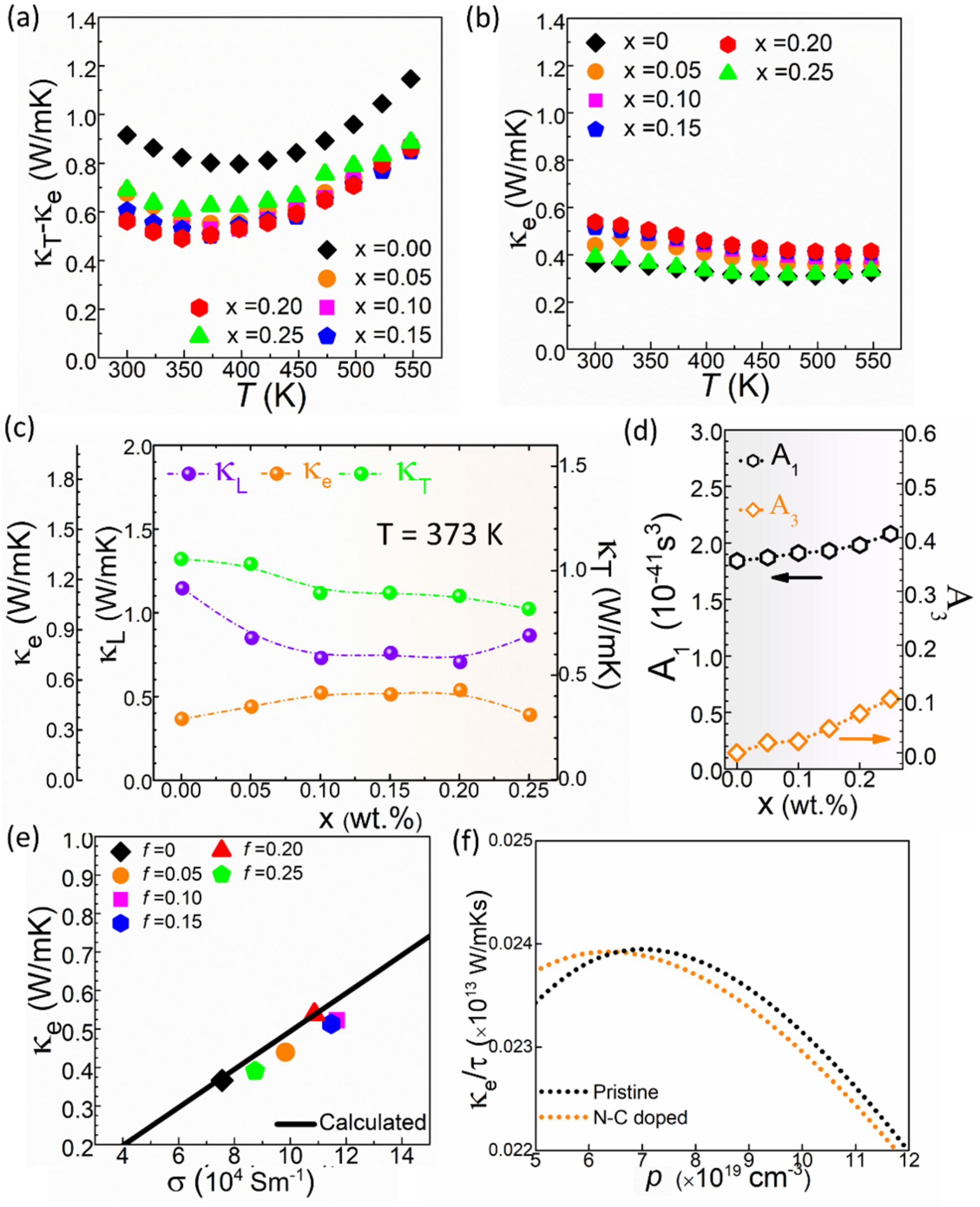

Fig. S12 (a) Experimental $\kappa_L(T)$ values as a function of x; (b) temperature dependent experimental κ_e values; (c) comparative view of experimental κ_L, κ_e, and κ_b values (at 373 K) upon x; (d) derived preset parameters A_1 and A_2 for calculated κ_L via Debye-Callaway model; (e) dependency of electric thermal conductivity κ_e on σ (at T= 300K) (where the symbols are the experimental data set); (f) DFT driven κ_e scaled by relaxation time (κ_e /τ) for N-C doped system shows a dependence of p for pristine and doped specimens.

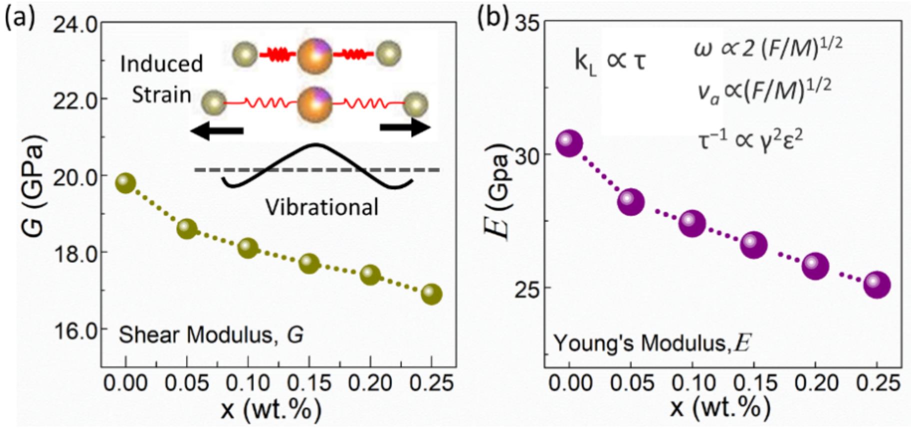

Fig. S13: (a) N-C doping dependent variations in Shear modulus (*G*); (b) Young Modulus (*E*).

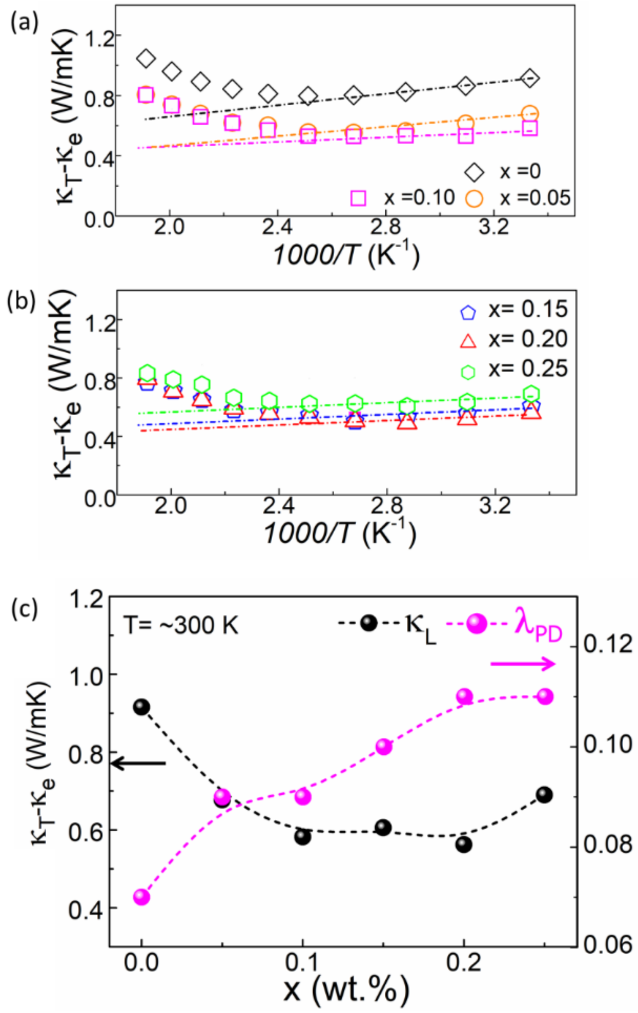

Fig. S14 (a-b) 1/*T* (K^{-1}) dependent experimental κ_b values; (c) the variation trends in lattice thermal conductivity and Peierls distortion parameter for all doped samples.

Supplementary Note 4: Thermal transport and ZT

The present N-C doping substantially reduces κ_T (Fig. 6). κ_T of all nanocomposite samples ($0.05 \leq x \leq 0.25$) is smaller compared to pristine. It can be noticed that κ_T declines as x increases from x=0 to x=0.20. However, at x =0.25, κ_T upsurges by reason of intensive involvement from carriers (as shown by Fig. 6a). In spite of bold intrinsic anharmonicity in $Bi_{0.4}Sb_{1.6}Te_3$ framework (that support the extensive Umklapp phonon−phonon scattering in the structure) the substantial decline in κ_L and κ_e values can be attributed to the induced scattering centers for wide frequency phonons (as depicted in Fig. S12).

Furthermore, the theoretical κ_L values of composite samples were calculated over the entire temperature range to confirm the contributions of various phonon scattering centers via Debye-Callaway model. As shown in Fig. 6b, the simulated κ_L curves by means of U + N + PD + EP + GB + ND mode can quantitatively predict the experimental data of $\kappa_T - \kappa_e$ for doped samples. Obviously, at high temperature, the deviance in the simulated κ_L is primarily owing to κ_b in $\kappa_T - \kappa e$. Moreover, the spectral lattice thermal conductivity (κ_s) can quantitatively clarify the specific scattering mechanism contributing for phonons in κ_L. Herein, the contributions from Umklapp processes (U), point defects (PD), electrons–phonon (EP), grain/phase boundaries (GB), nano dislocation & strains (ND) based scattering centers on phonon transport is determined, as followed;

$$\kappa_S = \frac{4\pi\, {k_B}^4\, T^3}{\kappa_S h^3}\, \tau_T \frac{\chi^4 \exp(\chi)}{[\exp(\chi) - 1]^2} \qquad (S1)$$

χ symbolize reduced phonon frequency (expressed as; $\chi=\hbar\omega/KBT$), v_S stands for average sound velocity and τ_T represents total phonon relaxation time. τ_T is articulated by the following equation

$$1/\tau_T = 1/\tau_U + 1/\tau_N + 1/\tau_{PD} + 1/\tau_{EP} + 1/\tau_{GB} + 1/\tau_{ND} \qquad (S2)$$

where τ_U, τ_N, τ_{PD}, τ_{EP}, τ_{GB}, and τ_{ND} stand for relaxation time related to U-and N-process (U+N) scattering, vacancies/alloy defects (point defects, PD), electron-phonon scattering (EP), grain boundary (GB), and nano dislocation strain fields (ND) scattering. However, in present system, τ_{PD}, τ_{GB}, and τ_{ND} are significantly prominent in reduction of κ_L. Notably, the inclusion of phase boundary in the U + E + PD + GB mode provides relatively inferior κ_L compared to the U + N + PD mode. However, inclusion of nano dislocations causes significantly reduction in κ_L in the U + E + PD + GB + ND model. On this basis, it is concluded that the grain boundaries and nano dislocation are functioning for low, medium, and high frequency phonon scattering (as depicted in Fig. 6). DFT driven κ_e scaled by relaxation time (κ_e /τ) for N-C doped system shows a dependence of p for pristine and doped specimens (Fig. S12f). On account of the increased PF with a decrease of κ_T, the figure-of-merit values of all N-C doped specimens are improved than that of pure $Bi_{0.4}Sb_{1.6}Te_3$. The *ZT* values in $Bi_{0.4}Sb_{1.6}Te_3$ can be significantly improved by combining with the reduced thermal conductivity under nano-dislocations. As a result, intuitive coupled TE factors (σ, S, κ_T) are optimized in line individually.

Supplementary Note 5: TE properties repeatability and reproducibility

To ensure the reliability and accuracy of present results, multiple preparations and characterizations of the samples under consistent conditions were conducted. It confirms the repeatability and reproducibility for $Bi_{0.4}Sb_{1.6}Te_3$+x(N-C) (x= 0.15) specimens (see Fig. S15a-e).

Further, validation by a third party (Prof. Jun Mao from School of Materials Science and Engineering, Harbin Institute of Technology, Shenzhen) is performed to replicate characterization procedures. The third-party verification/validation on thermoelectric properties and experiments has shown a high degree of reproducibility in present work (Fig. S15f).

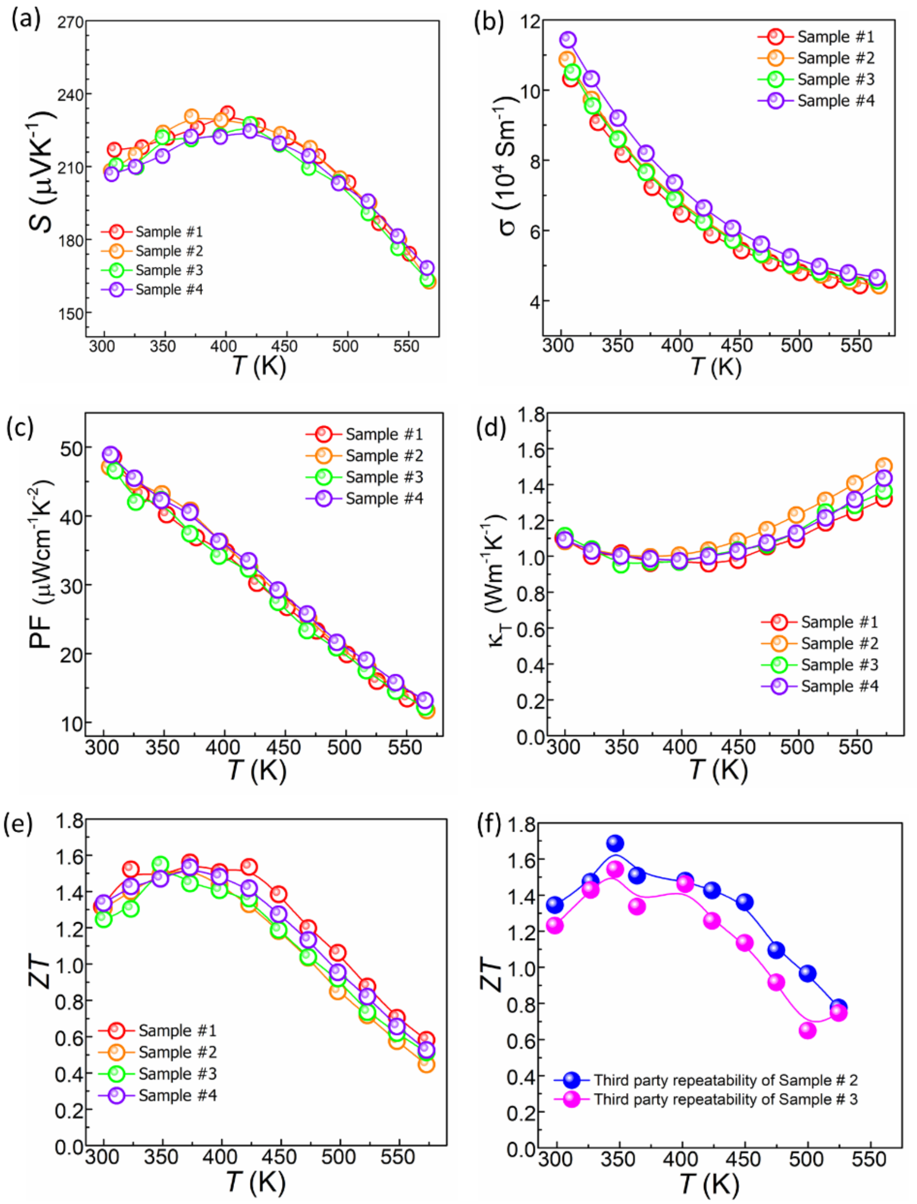

Fig. S15: Thermoelectric properties of $Bi_{0.4}Sb_{1.6}Te_3$+x(N-C) system (x= 0.15); (a) σ(*T*); (b) S(*T*); (c) PF(*T*); (d) total thermal conductivity κ_T(*T*); (e) thermoelectric Fig of merit (*ZT*) values; (f) external validation on thermoelectric figure-of-merit (ZT) evaluation for p-type $Bi_{0.4}Sb_{1.6}Te_3$+x(N-C) samples (x=0.15).

Supplementary Note 6: Device performance

Based on n-type Bi_2Te_3 and p-type N-C doped $Bi_{0.4}Sb_{1.6}Te_3$ (x= 0.15), a pair of p-n legs were assembled electrically in series and thermally paralleled (the components are displayed in Fig. S16a). On the hot side, Copper (Cu) alloy was used as the diffusion barrier and Ag was used as the solder layer. On the cold side, Cu worked as the diffusion barrier and a Sn–Bi alloy was used as the solder layer. The voltage, output power and conversion efficiency were measured by changing the current (I) under different temperature differences (ΔT) using a commercial PEM-2 testing system (ULVAC-RIKO, Inc.). The hot-side temperature was set as 350 K, 400 K, 450K and 500 K, while the cold-side temperature was kept at ~300 K. The measured results are shown in Fig. S16b-d. At a given ΔT, the power output increased with increasing current and reached a maximum value (P_{max}). Because of the superior TE properties of our material (N-C Doped $Bi_{0.4}Sb_{1.6}Te_3$) in the whole temperature range, our module with (6.1%, ΔT = 200 K) is among the best in comparison with other reported Sb_2Te_3-based modules (Fig. S16e). [3-10]

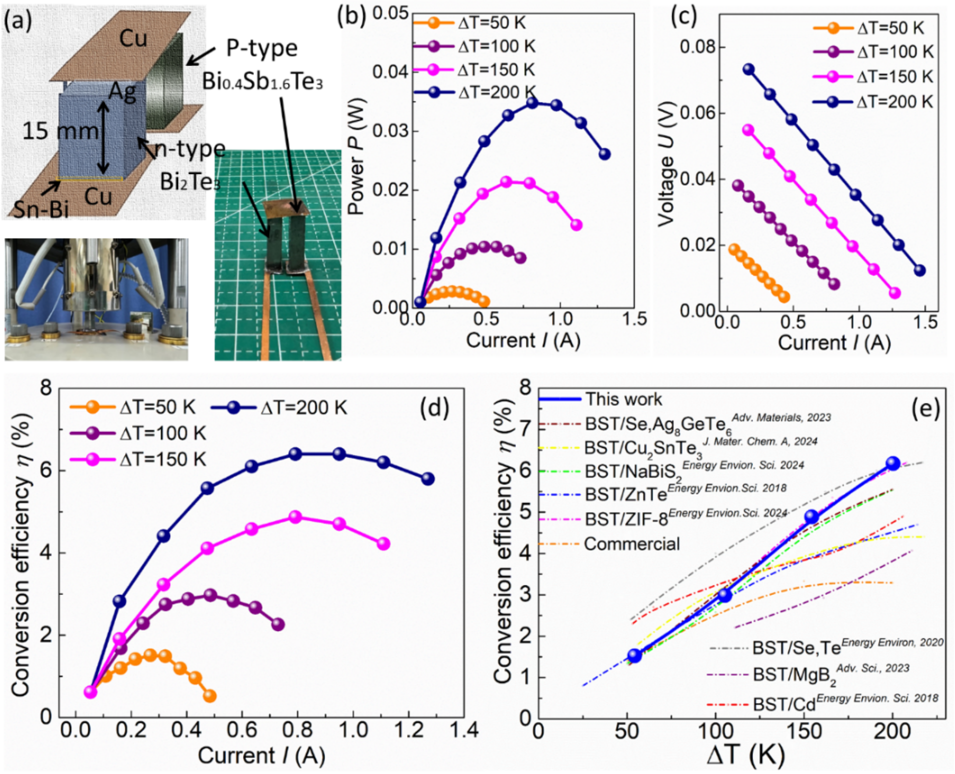

Fig. S16: (a) Design drawings and photograph of the TE power generation module; (b) output power; and (c) voltage as a function of current; (d) conversion efficiency of a pair TE power generation module as a function of current at different hot-side temperatures; (e) the energy conversion efficiency of the 2 leg TE module in this work and comparison reported values of Sb_2Te_3-based TE modules in the literature.[3-10]

Supplementary Note 7: Details of experimental method and simulations

Sample preparation: The N-C doped specimens were synthesized using a two-step process. Firstly, N-C doped porous carbon material was prepared. The synthesis method for PDAP preparation was taken from the previously reported work.[11] To prepare PDAP particles, 1 g of sodium hydroxide and 5.45 g of 2,6 diamino pyridine were dissolved in distilled water (400 ml). Then, a mixture of 17.1 g of ammonium per-sulfate was added in distilled water with quantity of 100 ml followed by stirring of the resulting fusion for 12 hours at room temperature. The formed black solids were collected by centrifugation and rinse with distilled water three times. Finally, the particle proceeded to vacuum-drying at 70°C. The PDAP particles were pyrolyzed at 900°C for 3 hours under N_2 environment at 5°C/min. After pyrolysis at 900°C, it was transformed into nitrogen-doped carbon (N-C) based porous material.

To prepare N-C doped $Bi_{0.4}Sb_{1.6}Te_3$ compounds, high-purity Bi, Sb, and Te elements (~99. 99%) were weighed and packed under vacuum in glass ampules according to the nominal compositions of doped $Bi_zSb_{2-z}Te_3 + \alpha C$ (α= 0.00, 0.10, 0.15, 0.20 wt.% at z = 0.4) and doped $Bi_zSb_{2-z}Te_3$ +x(N-C) (where x=0, 0.05, 0.10, 0.15, 0.20 and 0.25 wt.% at z = 0.4). The composite samples were prepared by melting stoichiometric amounts using two subsequent melting stages. Firstly, the glass ampules were melted at 1323 K with the rate of 2 K per-minute and kept at T=1323 K used for 12 hours, followed by a controlled cooling with the rate of 2 K per-minute. For second stage heating process, the glass tubes were annealed and kept under 773 K for 5 hours, followed by a controlled cooling with the rate of 2 K per-minute. By hand grinding, the molten samples were reduced to a fine powder in the micron range. Subsequently, Spark Plasma Sintering (SPS) process was then used to sinter and compact the micron-sized powders, and sintering was attuned for 15 minutes in vacuum under stress of 60 MPa at 723 K. This resulted in high-density pellets with at least ≥98% of the theoretical density.

Characterizations: The commercial ZEM-3 device (Model, ULVAC-Riko) was employed for electrical conductivity (σ) as well as Seebeck coefficient (S) analysis. The accuracy of resistivity and Seebeck coefficient measurements is approximately ±2% and ±5% uncertainty, respectively. The carrier concentration (*p*) was measured at room temperature (~300 K) by HL5500PC apparatus under magnetic induction of 0.5 T. The equation σ/(e. *p*) is used for the determination of the carrier mobility (μ). The *p* and μ values were measured under uncertainty of ±10% and ±12%, respectively. Total thermal conductivity (κ_T) was determined by means of the formula $\kappa_T = D_t \times d \times C_p$, where D_t signifies thermal diffusivity, *d* stands for density, and C_p is specific heat. The D_t values were analyzed using a Netzsch LFA467 equipment with the uncertainty of ±7%. To avoid overestimating, the D_t measurement was taken in the same direction as the resistivity measurement. Specific heat (C_p) for pristine samples was analyzed using differential scanning calorimeter (Model: Netzsch-DSC404), while Archimedes' method was used to find *d*. Room temperature (~300 K) sound velocity (v_a) was measured by determining longitudinal and transverse parts of sound velocities through a pulse-receiver (oscilloscope, Olympus-NDT) under uncertainty of ±1%. The ZT accuracy is estimated at ±10% uncertainty. The bulk samples were further examined for crystal structure by X-ray diffractometer (model: Riguku, Japan with λ = 1.5406 Å). Further, slow scan XRD data was used to carry out simulated crystallographic studies by Rietveld refinement method through the Generalized Structural Analysis System (GSAS-II) package. The newly cracked specimens were used for microstructure investigations using Field Emission Scanning Electron Microscopy (Model: Ultra 55-Zeiss). The investigated details for microstructural level variations of doped specimen were carried out by transmission electron microscopy (Model: JEOL-F2010).

Simulation methods: In the Vienna Ab initio Simulation Package code, First-principle based Density Functional Theory simulations were accomplished through the Projector Augmented Wave method. Fully relativistic Perdew-Burke-Ernzerhof practice was chosen to treat the exchange correlation interactions. In this work, all projected defects of element vacancies, anti-site and interstitial doping were simulated by a 2 × 2 × 1 supercell for both the pristine and doped systems. For atomic coordinates and ionic positions relaxation, the force convergence criterion and the total ground state energy were fixed at $0.02\ \text{eV}\ \text{Å}^{-1}$ and 10^{-5} eV. Cutoff energy of the plane wave was set at 400 eV. For pristine structure, the calculated band gap is well consistent with previously reported values. [12-18]

References

1. H. Ming, G. Zhu, C. Zhu, X. Qin, T. Chen, J. Zhang, D. Li, H. Xin and B. Jabar, *ACS Nano*, 2021, **15**, 10532-10541.
2. W. Ji, X.-L. Shi, W.-D. Liu, H. Yuan, K. Zheng, B. Wan, W. Shen, Z. Zhang, C. Fang and Q. Wang, *Nano Energy*, 2021, 106171.
3. Q. Zhang, M. Yuan, K. Pang, Y. Zhang, R. Wang, X. Tan, G. Wu, H. Hu, J. Wu, P. Sun, G.-Q. Liu and J. Jiang, *Advanced Materials*, 2023, **35**, 2300338.
4. Q. Pan, K. Pang, Q. Zhang, Y. Liu, H. Shi, J. Li, W. Zhou, Q. Sun, Y. Zhang, X. Tan, P. Sun, J. Wu, G.-Q. Liu and J. Jiang, *Journal of Materials Chemistry A*, 2024, **12**, 8785-8795.
5. Y.-C. Shi, J. Yang, Y. Wang, Z.-G. Li, T.-Y. Zhong, Z.-H. Ge, J. Feng and J. He, *Energy & Environmental Science*, 2024, **17**, 2326-2335.
6. R. Deng, X. Su, S. Hao, Z. Zheng, M. Zhang, H. Xie, W. Liu, Y. Yan, C. Wolverton and C. Uher, *Energy & Environmental Science*, 2018, **11**, 1520-1535.
7. W. Zhang, B. A. Al-Maythalony, F. Gao, F. Wu, W. Zhao, P. Xu, W. Zhang, C. Chen, Z. Shi, X. Wang, Y. Lou and B. Xu, *Energy & Environmental Science*, 2024, **17**, 5679-5690.
8. X. Hu, K. Nagase, P. Jood, M. Ohta and A. Yamamoto, *Journal of Electronic Materials*, 2015, **44**, 1785-1790.
9. C. Zhang, Q. Lai, W. Wang, X. Zhou, K. Lan, L. Hu, B. Cai, M. Wuttig, J. He, F. Liu and Y. Yu, *Advanced Science*, 2023, **10**, 2302688.
10. F. Hao, P. Qiu, Y. Tang, S. Bai, T. Xing, H.-S. Chu, Q. Zhang, P. Lu, T. Zhang, D. Ren, J. Chen, X. Shi and L. Chen, *Energy & Environmental Science*, 2016, **9**, 3120-3127.
11. Q. Chen, D. Shu, Z. Zhao, Z. Zhao, Y. Wang and B. Yuan, *Materials & Design*, 2012, **40**, 488-496.
12. M. Tan, W.-D. Liu, X.-L. Shi, J. Shang, H. Li, X. Liu, L. Kou, M. Dargusch, Y. Deng and Z.-G. Chen, *Nano Energy*, 2020, **78**, 105379.
13. S. Bano, D. K. Misra, J. S. Tawale and S. Auluck, *Journal of Materiomics*, 2021, **7**, 1264-1274.
14. M. Tan, X.-L. Shi, W.-D. Liu, M. Li, Y. Wang, H. Li, Y. Deng and Z.-G. Chen, *Advanced Energy Materials*, 2021, **11**, 2102578.
15. L. Hu, F. Meng, Y. Zhou, J. Li, A. Benton, J. Li, F. Liu, C. Zhang, H. Xie and J. He, *Advanced Functional Materials*, 2020, **30**, 2005202.
16. F.-X. Bai, H. Yu, D. Peng, H.-J. Pang, L. Yu, L.-C. Chen, J. Mao, Q. Zhang and X.-J. Chen, *Materials Today Physics*, 2023, **37**, 101200.
17. G. Yang, L. Sang, F. F. Yun, D. R. G. Mitchell, G. Casillas, N. Ye, K. See, J. Pei, X. Wang, J.-F. Li, G. J. Snyder and X. Wang, *Advanced Functional Materials*, 2021, **31**, 2008851.
18. B. Jabar, A. Mansoor, Y.-X. Chen, S. Jamil, S. Chen, G.-x. Liang, F. Li, P. Fan and Z.-h. Zheng, *Chemical Engineering Journal*, 2022, **435**, 135062.